McKelvey School of Engineering Theses & Dissertations

McKelvey School of Engineering

Winter 12-18-2018

Electroless Nickel Plating and Spark Plasma Sintering of nano ZrO2 for Mechanical Property Enhancement

Kunlong Jia
Washington University in St. Louis

WASHINGTON UNIVERSITY IN ST. LOUIS

School of Engineering and Applied Science

Department of Mechanical Engineering and Material Science

Thesis Examination Committee:
Dr. Shankar Sastry
Dr. Srikanth Singamaneni
Dr. Peng Bai

Electroless Nickel Plating and Spark Plasma Sintering

of nano ZrO$_2$ for Mechanical Property Enhancement

Kunlong Jia

A thesis presented to the School of Engineering
of Washington University in St. Louis in partial fulfillment of the
requirements for the degree of
Master of Science

December 2018

Saint Louis, Missouri

Contents

List of Tables

List of Figures

Acknowledgments

I would like to offer most sincerely thanks for the guidance from Dr. Sastry during my thesis. Thank you for the patience in advising me when I got loss.

I appreciate Abishek Venkatesan Iyer for leading the group during the first semester and guiding me in learning all the required techniques performing the research.

I am thankful for the help of George Li of SPS Nano Ceramics in consolidation experiments

<div align="right">

Kunlong Jia

Washington University in St. Louis

December 2018

</div>

ABSTRACT OF THE THESIS

Electroless Nickel Plating and Spark Plasma Sintering
of nano ZrO$_2$ for Mechanical Property Enhancement

by

Kunlong Jia

Master of Science in Mechanical Engineering

Washington University in St. Louis, 2018

Research Advisor: Professor Shankar Sastry

A new approach of combined electroless nickel plating (ENP) and spark plasma sintering (SPS) was used to determine the feasibility of fracture toughness improvement of ZrO$_2$. Nano-grained yttria stabilized zirconia (YSZ) particles of 100nm average diameter were coated with about 1-5 nm of nickel coating by ENP. To reduce nano particle agglomeration throughout the ENP process; vigorous agitation with an ultrasonic horn was used. The coated powder was characterized using Scanning Electron Microscopy (SEM), Energy-dispersive X-ray spectroscopy (EDX) and Transmission electron microscopy (TEM) to study the microstructure and coating characteristics. The coating was identified to be predominantly nickel and of 1 to 5 nm thickness. The plated powder was dried and consolidated by Spark plasma sintering (SPS) with sintering times significantly lower than used in conventional sintering processes. The solid compact was evaluated for mechanical properties. Hardness values were obtained from Vickers micro hardness indentations; fracture toughness was calculated by indentation-crack-length measurement and three-point bend test of notched samples; flexural strength was measured by 3-point bend tests. The measured hardness is comparable to the results found in the literatures. The coated and uncoated zirconia show significantly higher average fracture toughness compare to existing values.

Chapter 1: Introduction

Pure zirconia is known for its high melting temperature and chemical stability. It has three known phases: monoclinic (below 1170℃), tetragonal (between 1170℃ and 2370℃) and cubic above 2370℃ [1]. The volume changes caused by phase transitions from monoclinic to tetragonal to cubic induce large stresses, which lead to internal cracking upon thermal cycling [2]. However, the tetragonal or cubic phase can be stabilized by the addition of other oxides such as magnesium oxide (MgO), yttrium oxide (Y_2O_3, yttria), calcium oxide (CaO), and cerium (III) oxide (Ce_2O_3) [3]. Yttria stabilized zirconia (YSZ) has been chosen for this project because about 8-10 mol.% of yttria dopant can eliminate the disruptive phase change happening during the transition, converting it into a material with superior thermal, electrical, and mechanical properties. However, the cracks left inside the material, fewer than without the other oxide additions, still cause stress concentration under loading and result in low fracture toughness of the material. Several approaches have been attempted in earlier investigations to ameliorate the negative effects. The approaches studied thus far include transformation toughening [4][5], composite toughening [6-8], ductile phase toughening [9-10] and fine grain toughening [34]. In the present investigation a new approach of combined electroless nickel plating (ENP) and spark plasma sintering (SPS) was used to determine the feasibility of fracture toughness improvement of ZrO_2. The measured hardness is comparable to the results found in the literature [30]. The coated and uncoated zirconia show significantly higher average fracture toughness compared to the values found in the literature [29].

Chapter 2: Background

2.1 Yttria-stabilized Zirconia

Zirconium dioxide (ZrO_2, zirconia) exhibits a rare combination of outstanding thermal, electronic, mechanical and chemical properties [11]. It also shows fine ionic conductivity at high temperatures. These merits render zirconia's wide application as the base component of many materials in industry areas such as solid oxide fuel cells, refractory materials, functional ceramics, abrasives, and dental implants. However, its polymorphism restricts the use of pure zirconia at high temperatures [12]. As shown in Figure 2.1 [31], at room temperature, pure zirconia occurs in the monoclinic phase (m-zirconia) and transform to the tetragonal phase (t-zirconia) at $\approx 1150℃$, continuous heating above $\approx 2380℃$ results in the transformation to the cubic phase of the pure zirconia (c-zirconia). Since both t- and c-zirconia are denser than the m-zirconia, repeated phase transitions lead to cracking in the material and, consequent deterioration of its mechanical properties. Thus, stabilization at high-temperature phases is required for industrial applications. Many approaches have been studied and the stabilization is obtained by the additions to zirconia of a proper metal oxide. Among the additions, yttria is an effective stabilizer of the high-temperature zirconia phases giving rise to yttria-stabilized zirconia (YSZ) [13]. Two different amounts of yttria additions are mostly used, 8 mol.% addition of yttria in zirconia lattice can stabilize the cubic phase (c-YSZ), while 3 mol.% of yttria addition leads to metastable tetragonal phase (t-YSZ) below 1000 ℃.
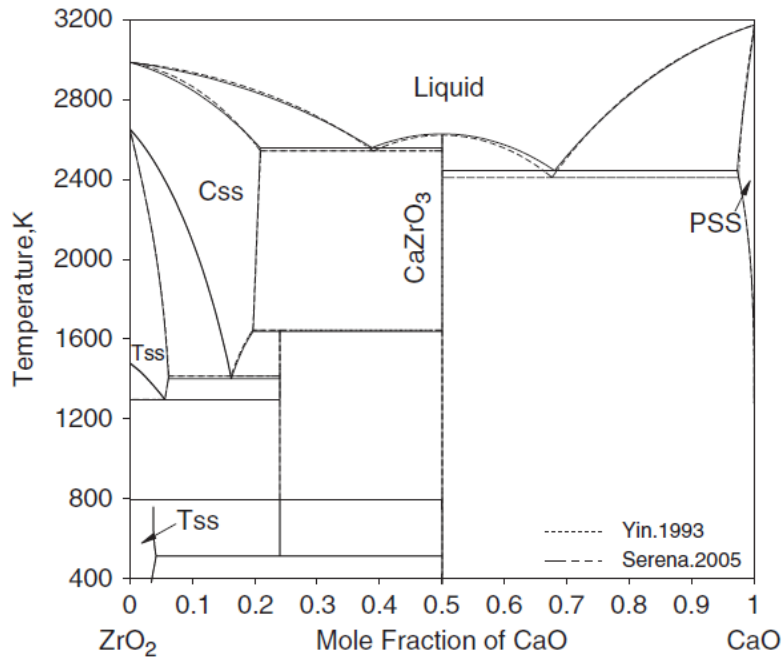
Fig. 2.1: Phase Diagram of ZrO_2 and CaO [31]

2.2 Use of nano-Zirconia

The choice of nanosize zirconia powder is based on the theory of fine-powder sintering. It is well-known that sintering beginning with smaller size particles may lead to improved functionality of resulting ceramics [15]. In particular, the sintering-induced mass transfer proceeds more efficiently and also the porosity of the ceramics becomes correspondingly smaller when sintering with nanopowders During sintering, particles will start to fuse together and cause grain growth, which deteriorates the mechanical properties. Nanosize particle sintering will compensate the negative effects to a great extent.

2.3 Ductile Phase Reinforcing

The method of introducing soft and ductile material to toughen intrinsically brittle materials has been used in the production of advanced composite materials and are generally named ductile phase toughening. [6] Experiments have proved that significant toughening can be achieved by incorporating ductile materials or fibers in low toughness ceramics, for example, Ni in MgO [7], Al in Al_2O_3 [8] and Mo in Al_2O_3 + ZrO_2 [9]. When the crack propagations start in the composite, the plastic deformation and stretching of the ductile reinforcements would produce closure traction over the crack surfaces. Additional far stress field required to

3

overcome the tractions before crack propagation continues in brittle phase contribute to the toughness increase of the matrix. The effect is also described as the bridging effect. Fig. 2.2 shows the bridging zone of Al_2O_3/Al composites [8]. When the bridging zone exists, residual stress present in the material can also contribute to the toughness by means of its influence on the initial crack opening force [10] (Fig.2.3).
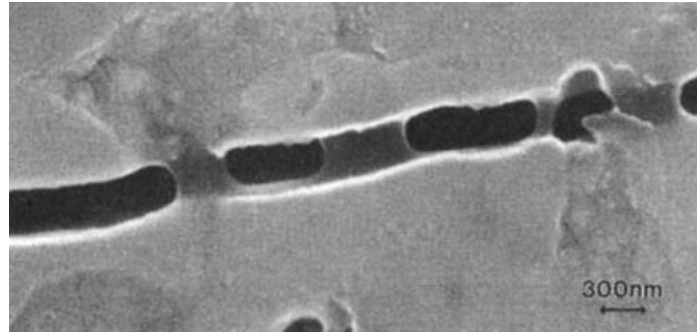
Fig 2.2 Bridge Al ligaments observed in Al_2O_3/Al composites [8]
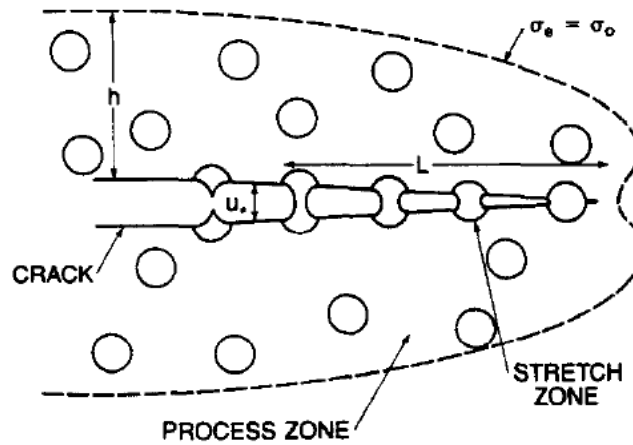
Fig 2.3 A schematic of the bridging process caused by plastically distorted ductile particles

K. S. Ravichandran [4] also conclude that the toughness of the composite is strongly influenced by the particle flow behavior, which can be represented by equation (2.1)

$$\Delta G_c = f \int_0^{u^*} \sigma(u)du \quad (2.1)$$

Where f is the area fraction of ductile material intercepted by the crack and u^* is the total crack opening when the ductile material fails (Fig. 2.3). The most important parameters are the constraint of the ductile particle, maximum flow stress, the displacement at maximum flow stress and the displacement at plastic

4

rupture of the particle. Higher maximum flow stress results in higher toughness. Lower constraint or higher rupture of the particle results in increasing composite toughness by enhancing matrix fracture toughness. The effect is due to the retaining of maximum bridging potential over a range of crack opening conditions.

2.4 Electroless Nickel Plating

Electroless plating bath contains a source of metal ions, reducing agent, complexing agent, stabilizer, buffering agent, wetting agent, and the process variables include bath, composition, temperature, and pH. The role of process variables is briefly summarized in Table 2.1. The deposition consists of the following steps: (i) cleaning (ii) surface modification (iii) sensitization (iv) catalyzing or activation [23]. Rinsing is required between the steps for cleaning the remaining chemicals.

Table 2.1 Components and parameters of bath and their functions

Component /Parameter	Function
Metal ion	Source of metal
Reducing agents	Supply electron to reduce the metal ions
Complexants	Prevent excess of free metal ions concentration
Accelerators	Accelerate the reducing agent and increase the deposition
Stabilizers	Stabilize the bath from decomposition by shielding catalytically active deposition
Buffers	Sustain the pH for long time
pH regulators	pH adjustment
Temperature	Energy for deposition

Electroless nickel plating process is an autocatalytic method in which the reduction of the nickel ions in the solution and the film deposition can be carried out through the oxidation of chemical compounds present in the solution itself, i.e., reducing agent, which supplies an internal current. [16] During the process, the nickel cation in the bath is reduced and deposited by receiving electrons delivered by the reducing agent, which is

oxidized on the deposition surface. The autocatalytic or chemical reduction of aqueous metal ions coated to a base substrate without passage of external current is referred to as electroless plating [17,18]. However, electroless plating different from other process used to deposit without current, such as immersion plating and homogeneous chemical reduction process (silvering). Such techniques differ from the autocatalytic deposition because the reducing agents are not required to reduce the metal ions to metal, as the base material itself behaves as a reducing agent [16]. Also, these techniques have not been widely used as their plating has poor adherence. Electroless nickel coating is superior over electroplating technique in several aspects. The advantages include the quality of the deposit, namely the physical and mechanical properties. It can also achieve a uniform coating on the surface as well as hard-to-access corners such as sharp edges and blind holes. Additionally, electroless plating offers extremely bright deposits when compared to electroplated bright nickel. The desirable properties can be varied by choosing different pH, temperature and composition of the bath. Electroless nickel coatings have acquired the highest commercial importance among the electroless coating processes. General categories of the electroless nickel coatings are shown in Fig. 2.4.

Electroless nickel coating

Pure nickel

Electroless nickel alloy coatings

(i) Alkaline, nickel-phosphorus

(ii) Acid, nickel-phosphorus

    a) 3-5%P (low phosphorus)

    b) 6-9%P (medium

    phosphorus)

    c) 10-14%P (high phosphorus)

(iii) Alkaline, nickel-boron

(iv) Acid, nickel-boron

(v) Ternary, quaternary alloy

    (polyalloy).

Electroless nickel composite coatings
(i) Nickel phosphorus
    composites (Ni-P-X)
(ii) Nickel-boron
    composites (Ni-B-X)
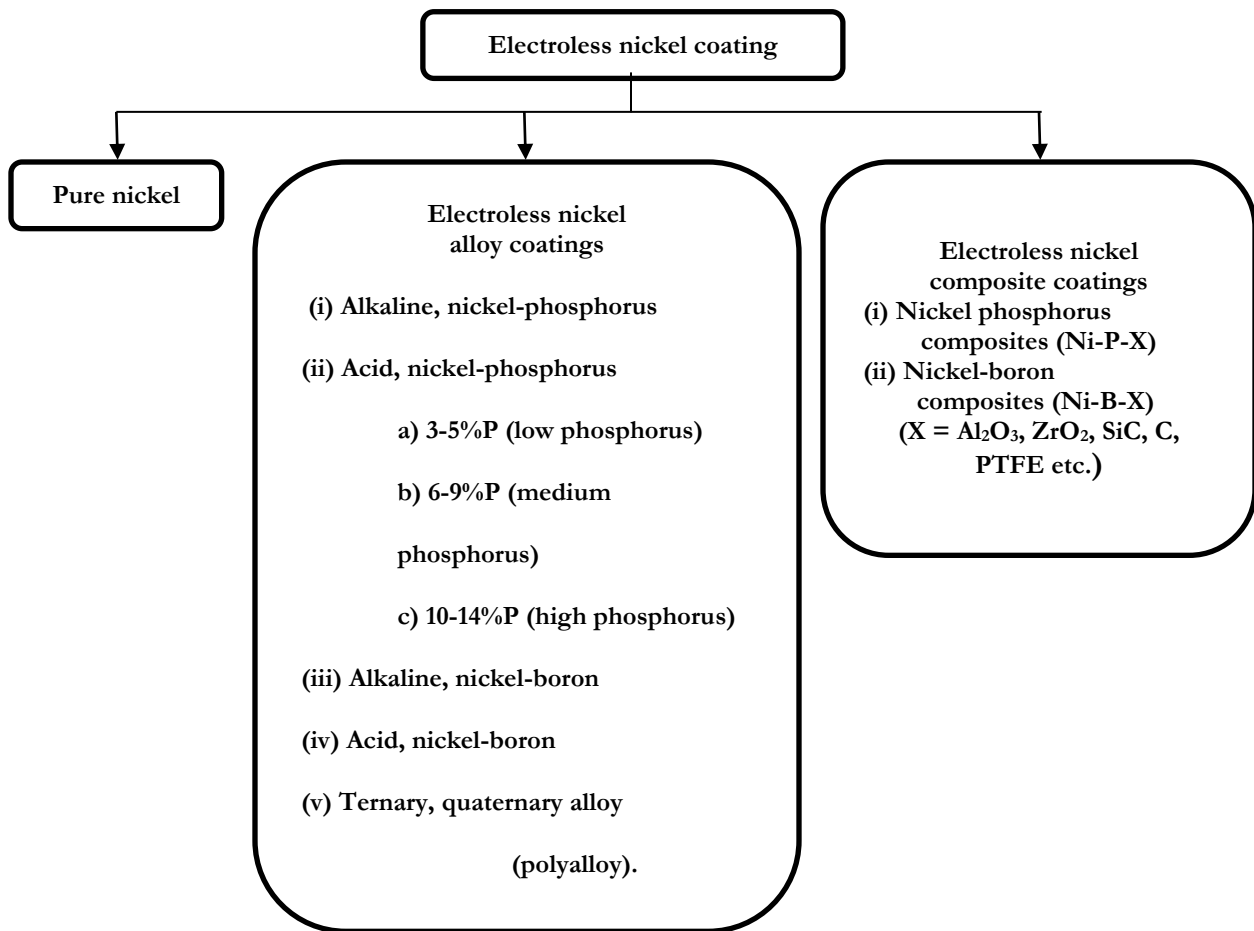(X = Al_2O_3, ZrO_2, SiC, C,
    PTFE etc.)

Fig 2.4 General categories of electroless nickel coatings

Commercialized reducing agents include sodium hypophosphite, amino boranes, sodium borohydride, and hydrazine. Sodium hypophosphite is adopted because of its lower cost and high corrosion resistance of the product. The reduction mechanism hypophosphite involves two reactions: (1) Hypophosphite ions are catalytically oxidized. (2) Nickel ions are reduced at the catalytic surface. A part of released hydrogen is absorbed onto the catalytic surface due to the anodic reaction. The absorbed active hydrogen then reduces the surface nickel ion (cathodic reaction). Some absorbed hydrogen reduces a small amount of the hypophosphite to water, hydroxyl ions and phosphorus ions. In general, 1 kg of sodium hypophosphite is needed to reduce 200 g of nickel, for an average efficiency of 37% [21,22]. Complexing agents are added to prevent the decomposition of solutions and to control the reactions so that it occurs only on the catalytic surface. Complexing agents also control the amounts of free electrons and act as a buffer solution to restrain the precipitation of nickel phosphite to maximize the amount of coating. Other pH buffers like ammonia, sodium hydroxides are also added periodically to neutralize the hydrogen ions. The complexing agent also affects the quality of the deposit, especially its phosphorus content and porosity. Typical complexing agents include citric, lactic, glycolic, proprionic acids, sodium citrate, succinic acid, etc. The addition of stabilizers can have harmful as well as beneficial effects on the plating bath and its deposit. In small amounts, some inhibitors increase the rate of deposition and the brightness of the deposit by controlling the amount of by-product (borate, hydrogen ions, dissolved metal) used which, decreases the plating rate [16].

Nanosize ceramic powders tend to agglomerate when mixed in water because of the tendency to reduce surface energy. Effective means of deagglomerating and dispersing are needed to overcome the process after wetting the powder. The ultrasonic breakup of the agglomerate structures in aqueous and non-aqueous suspensions allows the utilization of the full potential and or surface of nanosize powders [17].

Sensitization involves absorbing ions or molecules from a solution such as acidic Sn (II) or Sn (IV). An oversimplified chemical model assumes that the sensitizing ion can reduce the active metal from the catalyst solution, usually $PdCl_2$ (Au, Pt, Rh, and Ag solutions have also been used), for example

$$Pd^{2+} + Sn^{2+} \rightarrow Pd^0 + Sn^{4+} \quad (2.2)$$
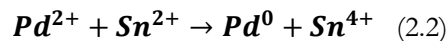
Activation is an essential step for surface pretreatment of ENP as it creates palladium nucleation sites on the surface of the substrate. The nucleation sites go through the reduction process as detailed above and initiate growth of nickel composition.

There are two kinds of bathing solutions: acid baths with a pH window between 4.9 and 5.2 and alkaline baths with a pH window between 10.2 and 10.8. Acid baths provide more stable reacting conditions while alkaline baths provide higher coating rates. Coating efficiency is the highest at around 85℃ and pH 10. The deposition rate is around 16 to 20 μm per hour depending on the specific bathing temperature, bath composition and substrate size. The chemical reaction during the process is shown below:

$$(H_2PO_2)^- + H_2O \xrightarrow{Catalyst\ \&\ Heat} H^+ + (HPO_3)^{2-} + 2H_{ini} \qquad (2.3)$$

$$Ni^{2+} + 2H_{abs} \rightarrow Ni + 2H^+ \qquad (2.4)$$

$$(H_2PO_2)^- + H_{abs} \rightarrow H_2O + OH^- + P \qquad (2.5)$$

$$(H_2PO_2)^- + H_2O \rightarrow H^+ + (HPO_3)^{2-} + H_2 \qquad (2.6)$$
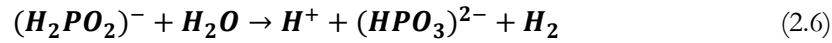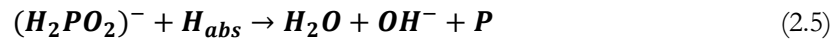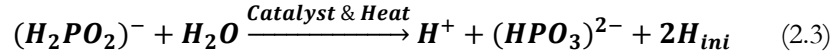
In equation (2.3), H_{ini} is surface hydrogen that initiates the nucleation process of autocatalytic growth of the electroless coating, which can be controlled by adequate substrate pre-treatment and adjusting bath condition.

2.5   Spark Plasma Sintering

Spark-plasma sintering (SPS) was invented in the late 1970s and has now become one of the most prevalent sintering techniques. The process is schematically illustrated in Fig. 2.5. The powders in graphite die are sintered directly instead of being pre-pressed prior to sintering using the conventional processing technique. After graphite die is placed in the furnace, two pistons acting as electrodes apply pressure on the upper and bottom surfaces. Due to the good electrical and thermal conductivity of the graphite die, adequate Joule heat is efficiently and quickly transferred to the starting powder under a relatively low voltage. Moreover, the heating rate can be as high as 1000 ℃/min, resulting from the adjustable current pulses (milliseconds). Although SPS shares some common factors with conventional hot pressing (HP) in the presence of heat and a uni-axial pressure across the specimen, SPS process has many advantages over HP. First, starting powder can be sintered using SPS in a few minutes, as opposed to hours for HP. Also, the temperatures needed to consolidate specimens to full density are significantly lower. These technology improvements open up the possibility of creating materials with nanoscale structural features. Finally, SPS is capable of sintering with ease and without sintering aids materials with relatively high melting points, such as tungsten carbide.
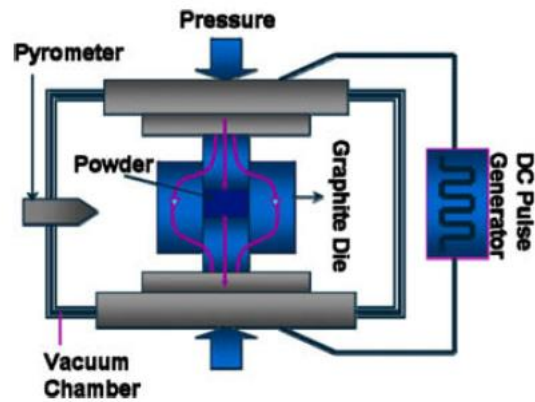
Fig 2.5: A schematic of the SPS process

The release of electrical energy through a porous powder compact breaks down the surface films and increases efficiency to mass transportation to neck. This effect will leave a clean grain boundary, increasing the surface area for sintering to take place and reduces sintering time dramatically, when compared to conventional sintering techniques. The local high temperature caused by spark discharge within the gap between the particles of material will lead to vaporization and melting of the surface of the powder during the SPS process and the forming of constricted shapes or "necks" between the particles. These necks will promote sintering into compacts to approximately 99% of the theoretical density as a result of the plastic transformation. Because the rapid temperature increase is limited to the surface area, better control of particle growth is achieved.

Chapter 3 Research Objectives

The goal of the project is to improve the fracture toughness of oxide-based ceramics in general and of ZrO_2 in particular by ductile phase reinforcement. The specific objectives of the current investigation are:

- Produce 1-5 nm thick uniform coating of ductile nickel coating on zirconia nanoparticles using electroless nickel plating.

- Produce nearly full-dense zirconia solid compact with ductile phase nickel reinforcement.

- Determine the hardness, fracture toughness and bend strengths of coated zirconia compact and evaluate mechanical property improvements over the uncoated zirconia compacts.

Chapter 4 Experimental Procedure

4.1 Materials

30nm and 100nm diameter 8 mol.% yttria stabilized zirconia nano powders were procured from Inframat® Advanced Materials™. The chemicals required for the sensitization, activation and bathing were purchased from Sigma Aldrich®. The chemicals were all analytical reagent grade. All nonproprietary solutions were prepared using deionized nanopure water.

4.2 Sample Preparation

20 g/L YSZ powder particles were first rinsed with deionized water and then mixed with 2 g/L $SnCl_2$ and 1 ml/L HCl solution for 30 minutes for sensitizing. The sensitized particles were then mixed with 0.3 g/L $PdCl_2$ for activating. After activating, the particle color changed from white to brown. Rinsing with nanopure water is required between each step. The chemicals required for the sensitization and activation are listed in Table 4.1

Table 4.1: List of Sample Preparation Chemicals and Compositions

Composition	Concentration
Tin chloride	2 g/L
Pallidum chloride	0.3 g/L
Hydrochloric acid	1 ml/L

4.3 Electroless Nickel Plating

Two kinds of plating bath recipes were used for coating: sulfite bath and chloride bath. The two batches of coated powders were compared

4.3.1 Sulfite Bath

The plating solution was heated to 85℃ on hotplate/stirrer prior to mixing with pre-treated powder and maintain at 85℃ throughout the process. The composition of the sulfite bath is listed in Table 2.2. The pH value of the mixture is kept at 5.4 by the addition of 1 g/L sodium hydroxide each time as the plating process goes on. The powder was kept dispersed through ultrasonication and stirred using a magnetic stir bar. The powder is rinsed with water for 3 times after plating for 1 hour and then dried. The washed powder was then characterized by JEOL-7001LVF Field Emission Scanning Electron Microscope.

Table 4.2: List of Sulfite Plating Chemicals and Compositions

Composition	Concentration
Nickel sulphate	30 g/L
Sodium citrate	24 g/L
Ammonium phosphate	45 g/L
Sodium hypophosphite	40 g/L
Thiourea	0.1 g/L

4.3.2 Chloride Bath

The temperature and pH condition were kept the same as sulfite bath, the chemical and compositions are listed in Table 4.3

Table 4.3: List of Chloride Plating Chemicals and Compositions

Composition	Concentration
Nickel chloride	35 g/L
Sodium citrate	24 g/L
Ammonium chloride	40 g/L
Sodium hypophosphite	40 g/L

An alternate recipe is listed in Table 4.4, the results of this batch is compared later.

Table 4.4: Alternate Recipe of Chloride Plating Chemicals and Compositions

Composition	Concentration
Nickel chloride	45 g/L
Sodium citrate	100 g/L
Ammonium chloride	50 g/L
Sodium hypophosphite	8 g/L

4.4 Powder Consolidation by Spark Plasma Sintering

Spark plasma sintering was carried out at SPS Nano Ceramic. The furnace used for SPS sintering has a 100kW capacity with a DC current of 10000 A and DC Voltage 10 V. The press capacity is 10 T, maximum temperature capability of 2300℃ and a vacuum of 5 Pa. Graphite molds are used to contain the powders and graphite rods are used as rams for the application of pressure on the powder. The electric power heats the powders by direct Joule heating along with conductive heat from the graphite mold. Consolidation is completed in short period of approximately 5 minutes. The whole SPS process is so fast that particle and grain coarsening are minimized. The process results in high-density compacts with the preservation of nanostructure. For coated YSZ powders, each batch weight is 17.5 g to achieve the compact disk thickness of at least 3 mm with 30 mm diameter for best result in Vickers hardness testing and three-point bend test. The batch weight is 35 g for uncoated powder for the thickness of 6 mm. The powder was sintered at 1400℃ for 8 minutes for uncoated powders and 3 minutes for coated powders because of different weight. Sintering pressure is set as 80 MPa and heating rate is 1000℃/min. The sintered compact was cut by diamond saw into 3 pieces of 20 mm or longer for 3-point bend test and two smaller pieces for cross-section vickers hardness test.

4.5 Microstructural Characterization

Microstructural characterizations were conducted at IMSE department and NRF of WUSTL. A small quantity of coated powders was dispersed into 1 ml acetone because dry powder surface tension is enormous, and particles tend to agglomerate and make it difficult to distinguish individual particles. Then the solvent is sonicated for best dispersion before SEM. Silicon wafer was used as the sample substrate for better

conductivity with ceramic samples and for better possibility to observe individual particles. A micropipette was used to deposit a small droplet on a silicon wafer. After the solvent evaporated, the sample was ready for SEM.

4.6 Mechanical Property Measurements

The micro hardness of the samples was measured in accordance with ASTM E384-16 with Phase II Vickers Hardness Tester and the fracture toughness was calculated from the indentation crack lengths measured under an optical microscope. The microhardness measurements were obtained by taking the mean of hardness values taken from 5 different areas for each sample. The hardness was calculated by the following equation:

$$\mathbf{HV} = \frac{\mathbf{1.8544F}}{\mathbf{a^2}} \left(\frac{\mathbf{kgf}}{\mathbf{mm^2}}\right) \quad (4.1)$$
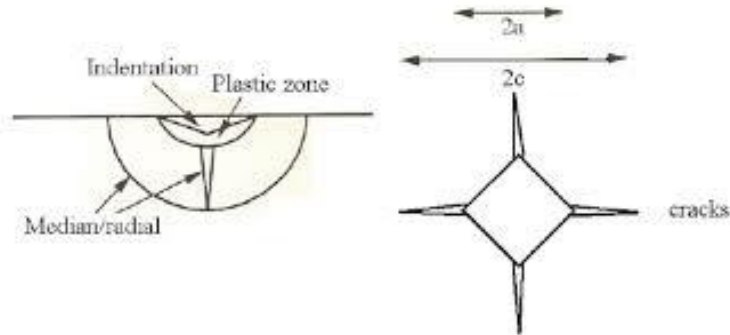

Fig. 4.1 An example of indentation and cracks

Fracture toughness values were determined using indentation crack length measurements technique. A sample picture of the crack and indentation is shown in Fig 4.1 [34]. The mounted specimens were subjected to different indentation loads from 10 kgf to 50 kgf. The indentation load of 50 kgf was the only load at which indentations were seen proving that the materials of the samples had high hardness values. The Young's modulus E was assumed to be 2 GPa. The value of crack length c was taken from the center of the indentation and the fracture toughness K_{IC} was calculated using the Palmqvist fracture toughness equation

$$\mathbf{K_{IC}} = \mathbf{0.016} \left(\frac{E}{H}\right)^{\frac{1}{2}} \frac{F}{c^{\frac{3}{2}}} \quad (4.2)$$

14

where K_c is toughness (MPa*m$^{1/2}$), E is Young's modulus (MPa), H is hardness (H$_V$), F is indentation load (kgf/mm^2), and c (c=l+a) is crack length measured from the center of indentation to the crack tip (micrometers). A three-point bend test fixture was mounted on the lower platform of a screw driven Instron machine. The load was applied on the specimen with a specially machined upper ram to produce three points bending load conditions. The support span was 16.5 mm. Tests were conducted at a crosshead speed of 0.008 mm/s, and load vs. deflection data up to specimen failure was obtained. Flexure stress-flexure strain values were calculated using equations (4.3) and (4.4), stress-strain curves were plotted and yield stress, fracture strength, and strain for fracture were determined.
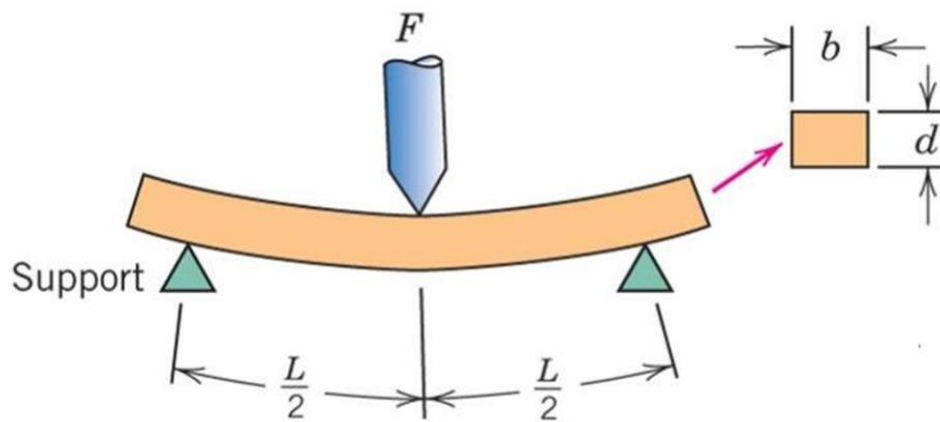

Figure 4.2. Three-point bend flexure test

$$\text{Flexural Stress} = \frac{3FL}{2bd^2} \quad (4.3)$$

$$\text{Flexural Strain} = \frac{6Dd}{L^2} \quad (4.4)$$

Where,

- P = load at a given point on the load deflection curve, (N)
- L = Support span, (mm)
- d = Width of test beam, (mm)
- W = Depth or thickness of tested beam, (mm)
- D = maximum deflection of the center of the beam, (mm)

.

Chapter 5 Results and Discussion

5.1 Microstructures

5.1.1   TEM and EDX of Chloride Bath Coated Powder

Fig. 5.1 shows the TEM image of the coated particles, where the dark regions are zirconia particles and light regions around the particle is the nickel coating. The TEM micrographs indicate that the coating thickness is around 1nm.
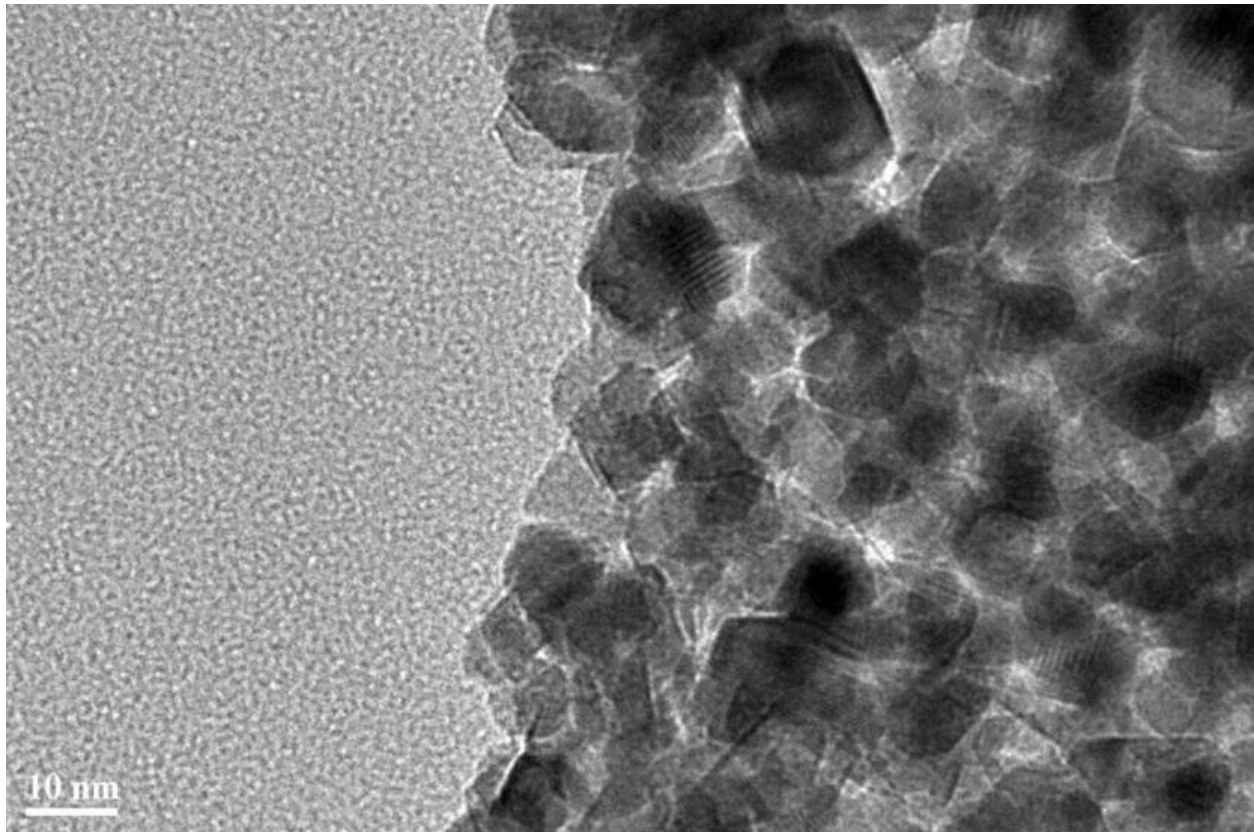
Fig. 5.1: TEM micrograph of nickel-coated YSZ powder (10nm scale)

Fig. 5.2: TEM micrograph of nickel-coated YSZ powder (2nm scale)

Fig. 5.2 showed the grains of the coated powders, which is presented as the grids in the picture. The contrast of dark region to bright region shows the different of conductivity due to nickel coating.
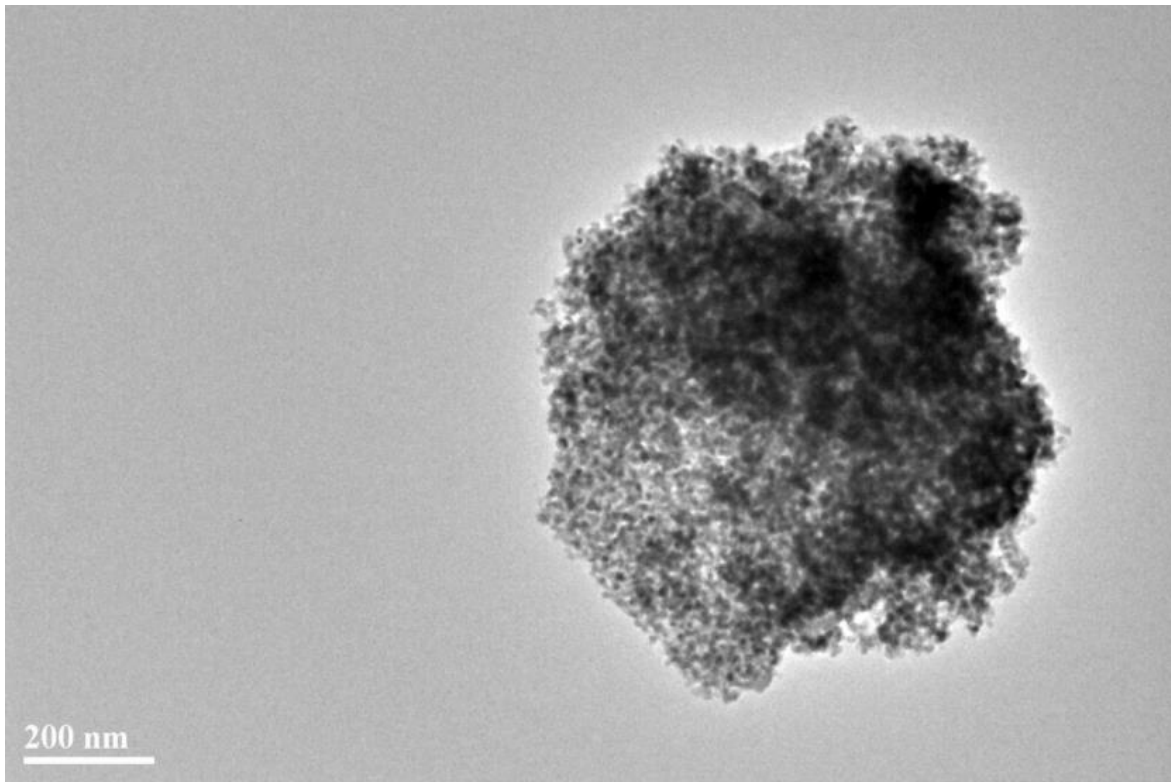
Fig.5.3: TEM micrograph of nickel-coated YSZ powder (200nm scale)
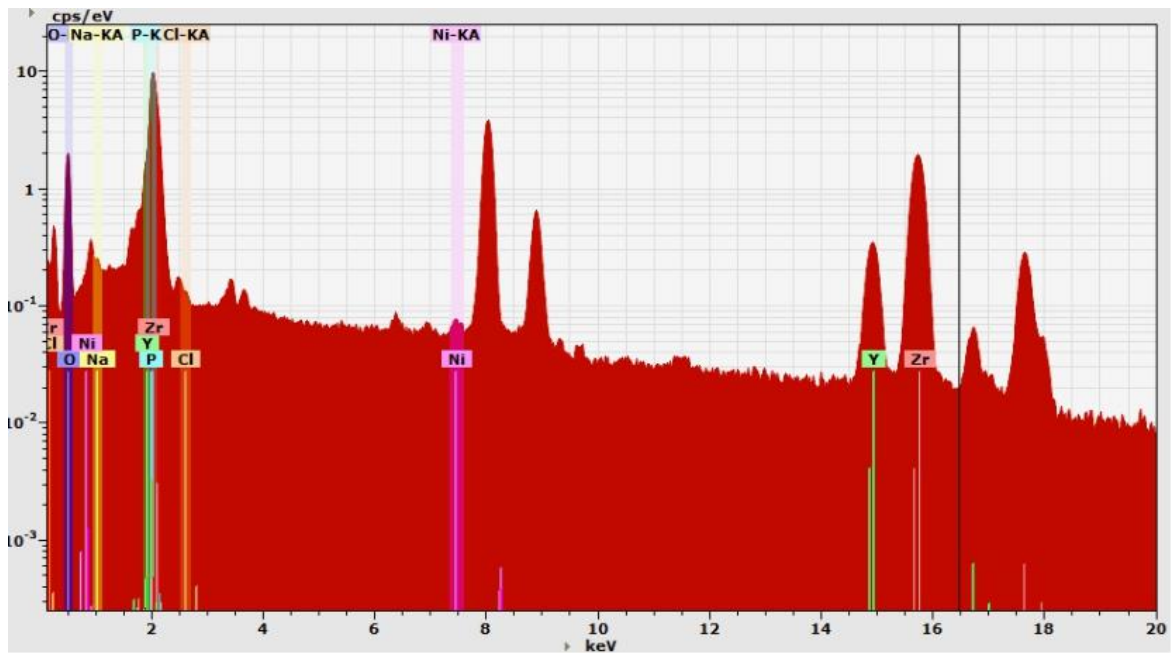
Fig. 5.4: EDX spectrum of nickel-coated YSZ powder
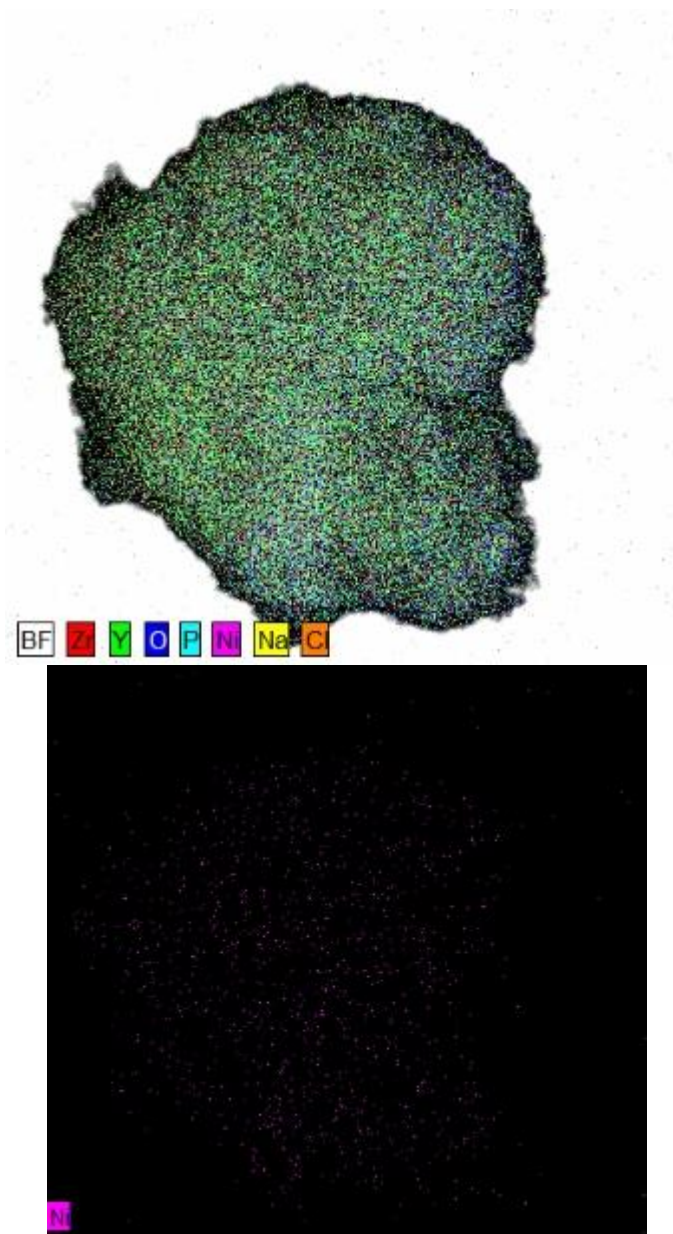
Fig. 5.5: Elemental mapping (Cl) of (a) nickel distribution (b)zirconium distribution

Fig. 5.4 is the EDX picture of the region shown in Fig.5.3. Primary Kα peaks of zirconia, yttria and nickel are clear evidence of successful nickel coating. Fig. 5.5 (a) and (b) are the elemental maps of all elements and nickel. We can observe that there is a uniform distribution of Ni in the region being analyzed.

5.1.2 SEM and EDX of Sulfite Bath Coated Powder
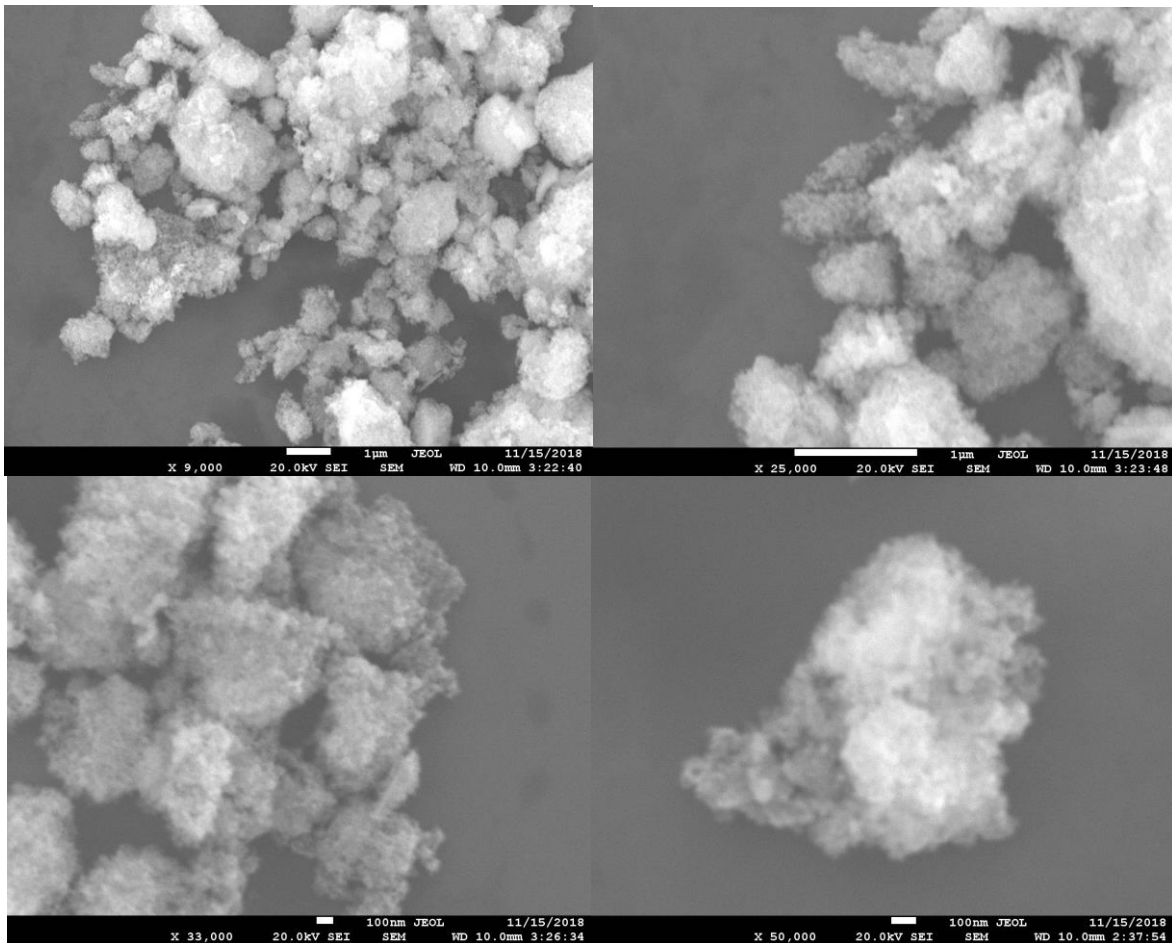
Fig. 5.6: SEM micrograph of sulfite nickel coated powder under (a) 9000 (b) 25000 (c) 33000 (d) 50000 magnifications

Fig. 5.6 shows the SEM micrographs of coated powder prepared with sulfite bath. A clear site of nickel deposition is shown in all particles presented. Particle size growth is also observed as a result of the coating.
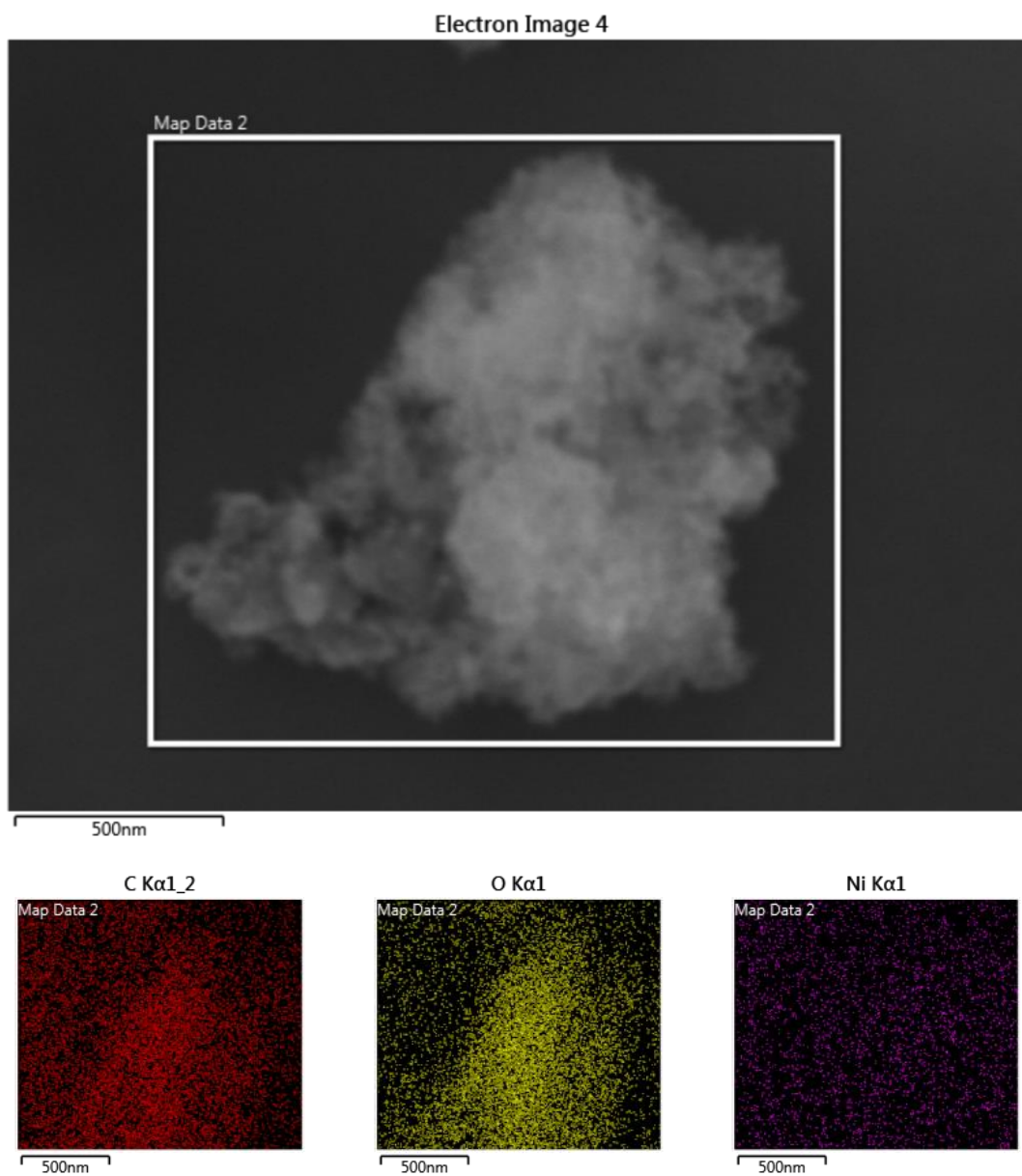
Fig. 5.7: EDX of coated powder (sulfite bath) with elemental mapping

It is evident in Fig. 5.7 that there is more nickel present in the sulfite bath coated YSZ particles when comparing to Fig. 5.5. Where is also supported by the observation of nucleation sites on the particle surface in Fig. 5.7.

5.1.3 SEM of Alternate Chloride Bath Coated Powder and Compact
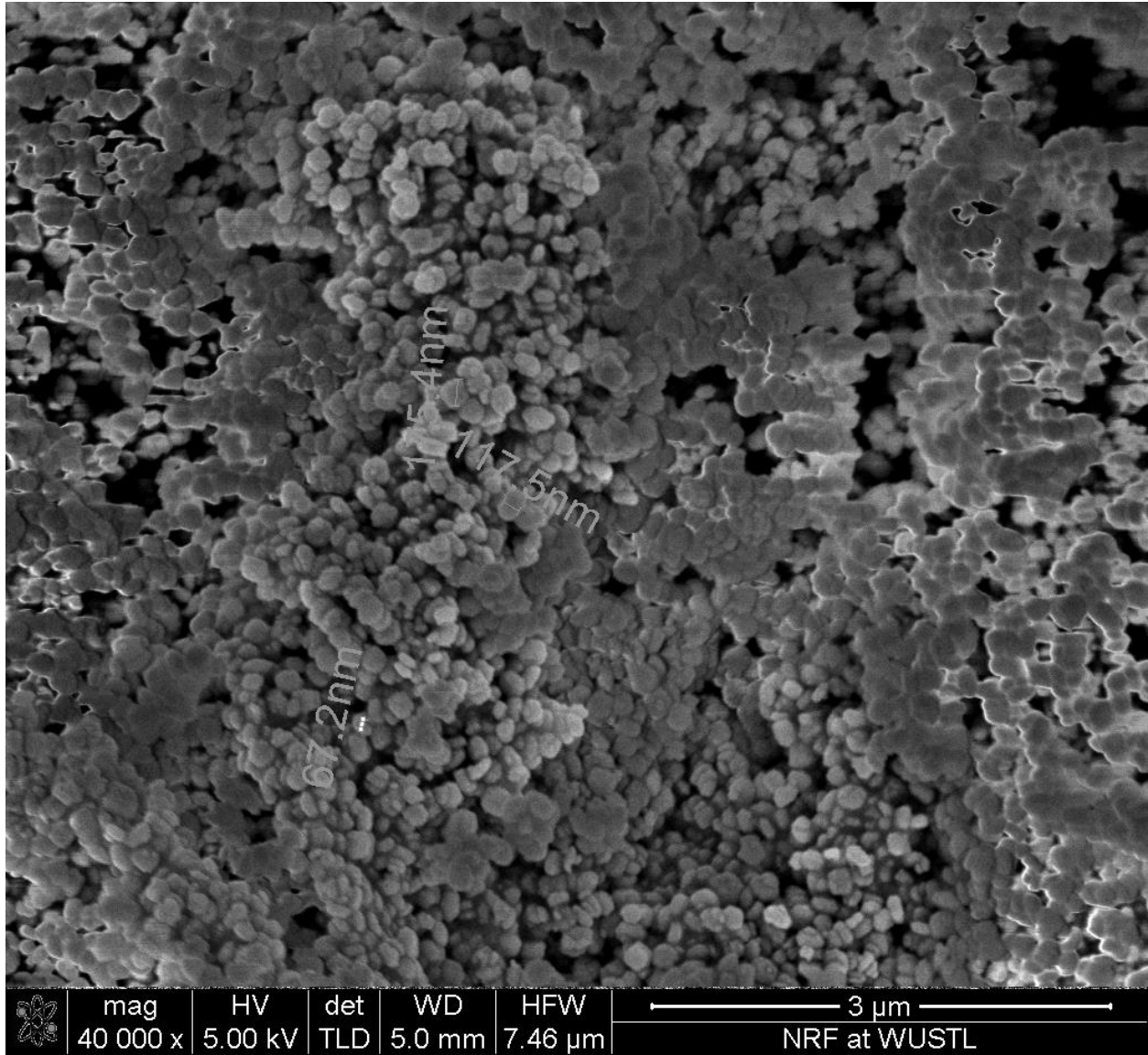
Fig. 5.8: SEM micrograph of alternate chloride batch nickel-coated YSZ powder

mag	HV	det	WD	HFW	5 μm
20 000 x	10.0 kV	ETD	5.2 mm	14.9 μm	NRF at WUSTL
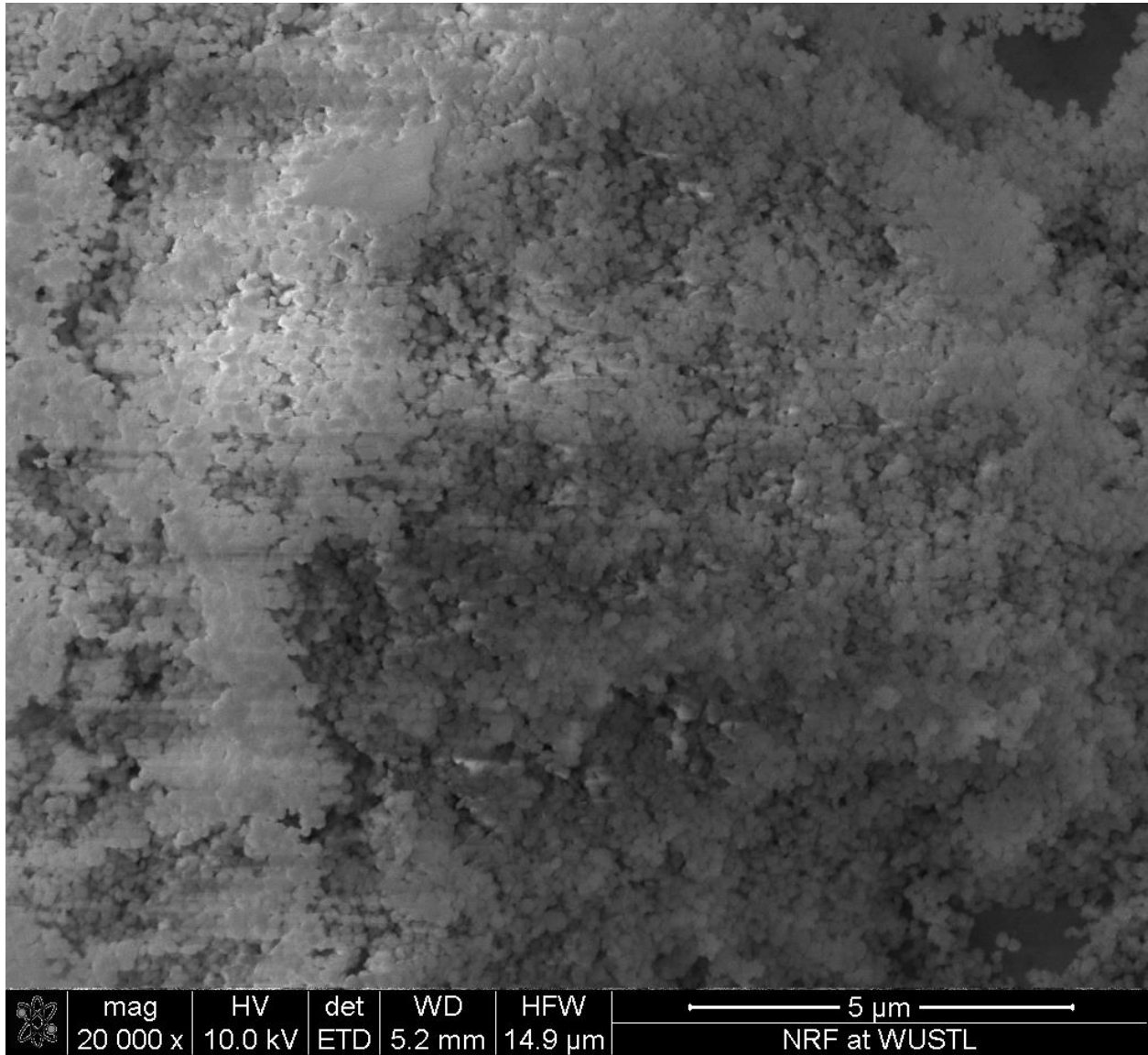
Fig. 5.9: SEM micrograph of alternate chloride batch nickel-coated YSZ compact (5μm scale)
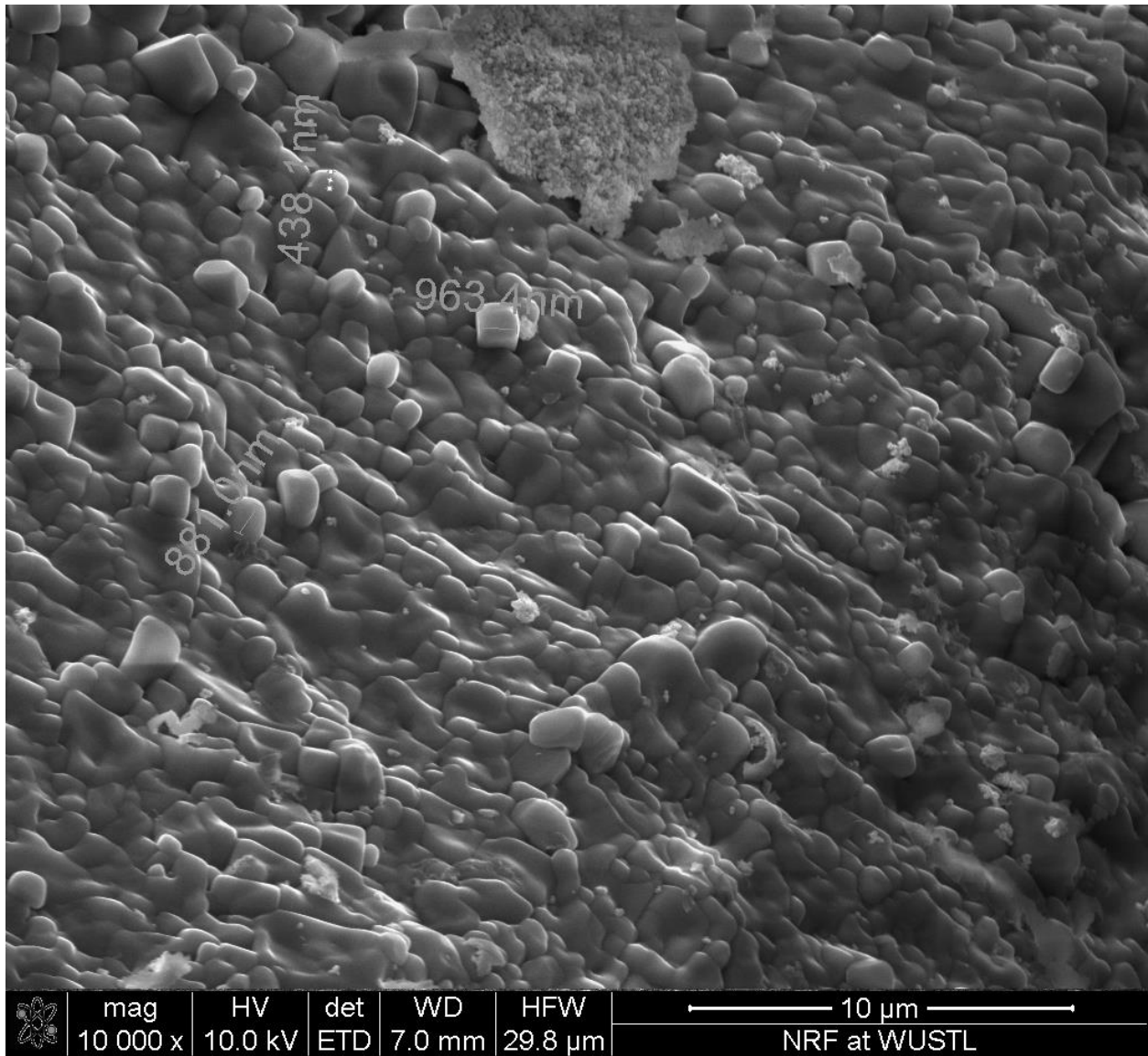
Fig. 5.10: SEM micrograph of alternate chloride batch nickel-coated YSZ compact (10µm scale)

As Fig. 5.8 shown, the coated YSZ particles size range from 67.2 nm to 175.4 nm, which is within the allowable range. Sign of nickel coating can be evidenced by the light range shell around the dark region of particles on the lower right corner and top left corner. Fig 5.9 shows that the compact is sintered well by SPS, but there are still porosities shown in some region. As Fig 5.10 shown, the sintered particles are within the range from 400 nm to about 1µm. Compare to the particle sizes shown in Fig 5.8, the grain size growth is from about 3 times to 15 times and still within nanosized range after sintering. The nanosized grains lead to a better result of fine grain toughening.

5.1.4 Optical Micrographs of Sintered Samples

Fig. 5.11 shows the comparison between coated (Cl) and uncoated YSZ solid compact surface after SPS. The coated sample showed less porosity, which demonstrates that coated YSZ achieves a higher density than the uncoated YSZ. The result is supported by the hardness measure based on Vickers hardness test on the two samples (Fig. 5.12 (a) and (b)).
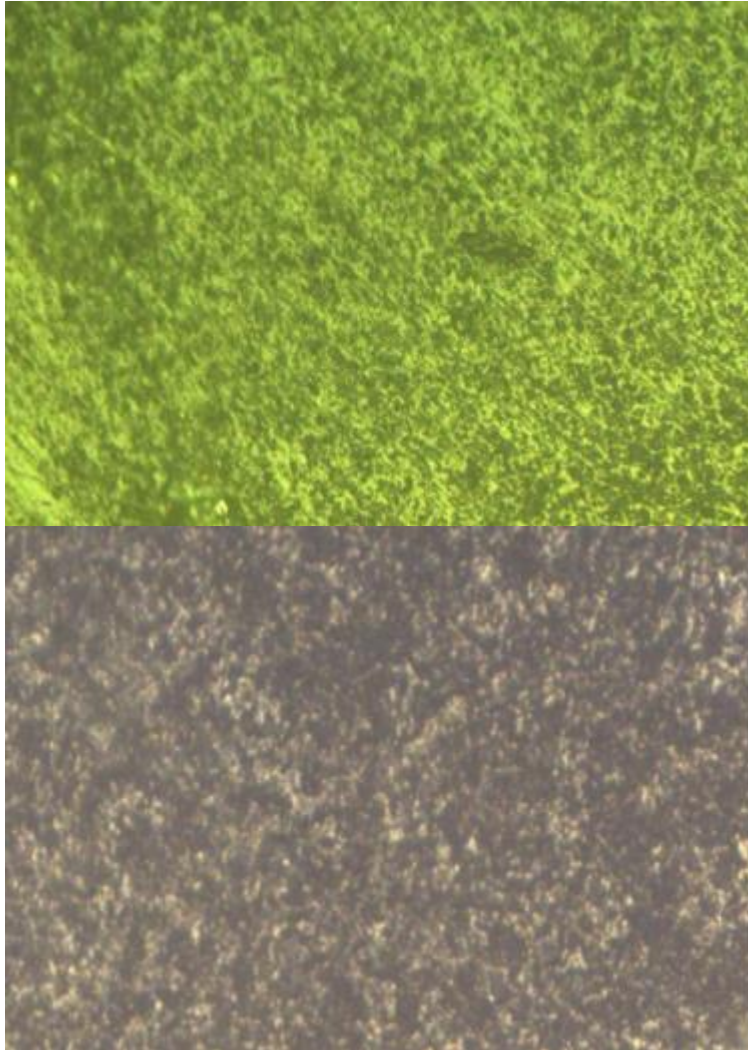
Fig. 5.11: Optical photograph of SPS (a) coated (Cl) (b) uncoated YSZ surface (200x magnification)
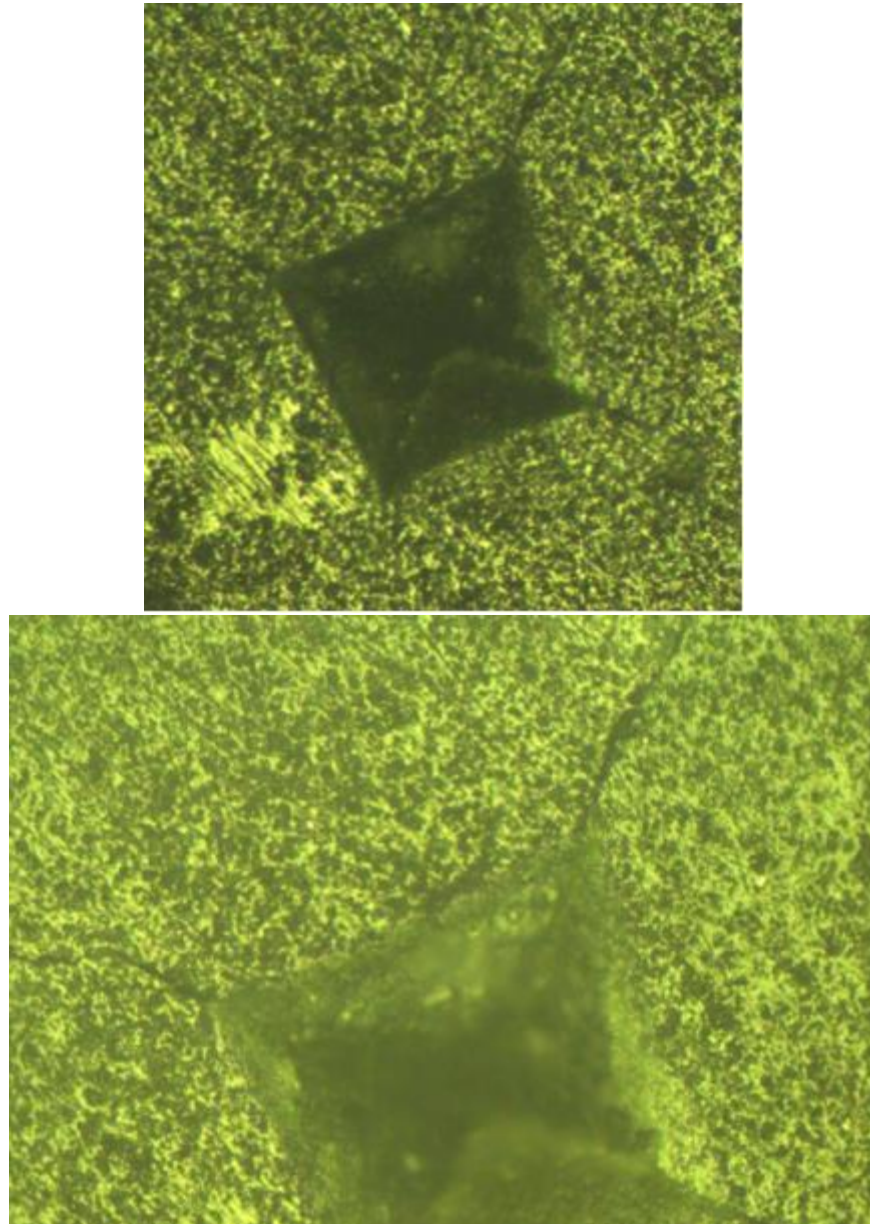
Fig. 5.12: Example of optical photographs of indentation of sintered YSZ (a) 100x magnification (b) 200x magnification

5.1.5 Fracture Toughness and Bend Strengths

Six indentations were taken on the polished cross-section of the sintered sample and the highest and lowest measurements were discarded. The mean micro hardness of uncoated YSZ is 8.5263 GPa while that of

coated (Cl) YSZ is 11.4025 GPa as presented in Table 5.1. Table 5.2 shows the fracture toughness comparison between coated and uncoated samples. The coated zirconia fracture toughness is 1.85 times higher than uncoated batch. Zadeh et al. measure a fracture toughness range of 3.34 to 3.77 MPa · mm$^{1/2}$ for 5 different zirconia [29]. The average fracture toughness of 4.865 from uncoated batch shows a significant increase. M. Turon-Vinas et al. obtained fracture toughness of 8.2 MPa · mm$^{1/2}$ for 12Ce-TZP zirconia and 8.0 MPa · mm$^{1/2}$ for Ce-TZP/Al$_2$O$_3$ zirconia [32]. The coated and SPS powder exhibit fracture of 9 MPa · mm$^{1/2}$, which is about 11.1% higher. The hardness of coated zirconia is about the same as the commercial zirconia values, which ranges from 10.7 to 12.3 GPa [33]. This result exceeds expectation for that the ductile phase typically reduces the hardness of the composite for Ni-P coating as observed in experiments [23]. However, the hardness could be enhanced by heated to 300℃ for 10 minutes, the reason for this observation is not clear but could probably be attributed to the formation of intermetallics [23]. Thus, the result showing the hardness of coated zirconia is not decreasing is satisfying. On the other hand, the uncoated zirconia exhibits lower average hardness values. There are several assumptions for the decrease: (1) the uncoated nano particles weren't dispersed by the ultrasonic horn, thus the agglomeration results in worse sintering which leads to low hardness. (2) the ENP process prepares the particles for better SPS results because the oxide film of the uncoated nanoparticles was broken down and the coated particles process much-enhanced conductivity. Also, we need to consider that the measurement of microhardness values of the composites using conventional testers only provide an average value for the hardness because of the dispersion of particles within the Ni–P matrix. The reinforcement of fracture toughness could be contributed to the bridge effect discussed earlier in the thesis provides a good explanation to the reinforcement. From the SEM micrographs, the coated thickness is about 5 nm and the particle sizes are 100nm, thus we could simplify the particle as layers of 5 nm of ductile Ni within layers of 100 nm of zirconia. The ductile phases would create plastic zones during crack propagation and slow down the process by bridging effect. Also, the nano-scale particle size would increase the number of transitions from brittle phase to ductile phase and significantly increase the number of plastic zones created on the crack propagation path to increase the far stress field required to break down the material and enhance the fracture toughness.

Table 5.1 Hardness of sintered uncoated and coated zirconia

Hardness, GPa	1st	2nd	3rd	4th	Average
Uncoated Zirconia	11.78	11.11	10.69	12.03	11.40
Coated (Cl) Zirconia	8.325	6.969	11.48	7.327	8.526

Table 5.2 Fracture toughness of sintered uncoated and coated zirconia

Fracture toughness, MPa $\cdot$ mm$^{1/2}$	1st	2nd	3rd	4th	Average
Uncoated Zirconia	2.529	3.188	6.414	7.327	4.865
Coated (Cl) Zirconia	9.508	8.838	7.916	9.747	9.002

5.1.6 Hardness and Fracture Toughness of the Alternate Batch

The hardness and toughness of the alternate batch were measured in the same way as above. The only difference is the hardness values were taken under the load of 2.4 N. The hardness value shows 24.5% enhancement comparing to the hardest commercial YSZ hardness which is 12 GPa. The comparison demonstrates that nanoscale grain size YSZ compact produced by SPS could enhance hardness effectively. The hardness of the coated batch is 14.6% lower than uncoated batch, the result is constant with the hardness reduction observation discussed in the previous section. However, these hardness values are still larger than that of commercial YSZ. On the other hand, the coated compact fracture toughness of this batch is significantly lower than that of the previous batch, while still higher than some of the commercial YSZ. Combining the increased hardness and decreased fracture toughness of the two batches and the bridge effect, we could conclude that the amount of nickel in the Ni-YSZ composite can slightly decrease hardness but can result in reinforcement of fracture toughness.

Table 5.3 Hardness of alternate batch sintered uncoated and coated zirconia

Hardness, GPa	1st	2nd	3rd	4th	Average
Uncoated Zirconia	15.48	15.46	14.26	14.54	14.94
Coated Zirconia	13.13	13.43	13.16	13.46	13.30

Table 5.4 Fracture toughness of alternate batch sintered uncoated and coated zirconia

Fracture toughness, MPa $\cdot$ mm$^{1/2}$	1st	2nd	3rd	4th	Average
Uncoated Zirconia	3.29	3.11	3.18	3.34	3.23
Coated Zirconia	4.61	4.67	3.95	3.88	4.28

Chapter 6 Summary and Conclusions

In this thesis, the coating microstructure is evaluated and the hardness, fracture toughness of sintered compact is measured and compared. As observed in TEM and SEM of zirconia particles, a thickness of 1nm is achieved for chloride bath and 10-30 nm thickness coating is achieved for sulfite bath, which indicates the ductile phase toughening on the brittle surface is successful. Sulfite bath exhibit thicker coating than chloride bath with the same pH, temperature and time conditions. The hardness value of 8.526 and 11.40 GPa is lower than 13.8 GPa tested by ASTM standard but fracture toughness of both batches is higher than existing results. The uncoated zirconia value comparison demonstrates that spark plasma sintering has positive effect on fracture toughness. The 85% increase of fracture toughness indicates that ductile phase toughening can significantly improve the mechanical properties of zirconia by the bridging effect. The alternate batch shows prominent hardness values of 14.94 GPa and 13.30 GPa for uncoated and coated compacts respectively; the fracture toughness is 3.23 MPa · mm$^{1/2}$ and 4.28 MPa · mm$^{1/2}$, which is still higher than many commercial YSZ. By comparing the two sets of hardness and fracture toughness values and consider the micrographs, we could conclude that (1) nanograin size is obtained and can effectively enhance hardness and fracture toughness. (2) increasing the amount of nickel presenting in the composite will slightly decreasing the hardness but can positively influence fracture toughness.

Chapter 7 Future Work

Firstly, the coated zirconia composite could be annealed to 300℃ for higher hardness because of the observation made by other scholars. The other reason is that nickel doesn't alloy zirconia at a lower temperature, thus the microstructure of coated zirconia should be studied by annealing. Secondly, as we observed from the discussion, more samples will be required to obtain more precise results for microhardness and fracture toughness. Furthermore, more study will be conducted on the crack surface of the composite to study the bridging effect and other reasons that could explain the reinforcement of the fracture toughness. Finally, more method to produce nickel-ceramic compacted will be tested and evaluated. Also, the same process of electroless nickel plating will be conducted on other ceramic material such as TiO_2, Al_2O_3 (Alumina), WC (tungsten carbide), etc. to compare the effect on mechanical properties.

References

[1] R.Stevens, 1986. Introduction to Zirconia. Magnesium Elektron Publication No 113

[2] Platt, P.; Frankel, P.; Gass, M.; Howells, R.; Preuss, M. (November 2014). "Finite element analysis of the tetragonal to monoclinic phase transformation during oxidation of zirconium alloys". Journal of Nuclear Materials. 454 (1–3): 290–297.

[3] Evans, A.G., Cannon, R.M. (1986). "Toughening of brittle solids by martensitic transformations". Acta Metall. 34: 761.

[4] K. S. Ravichandran, Acta metall, mater. Vol. 40, No. 5, pp. 1009--1022, (1992)

[5] Porter, D.L., Evans, A.G., Heuer, A.H. (1979). "Transformation toughening in PSZ". Acta Metall. 27: 1649.

[6] H. C. Cao, B. J. Dalgeleish, H. E. Deve, C. Elliott, A.G. Evans, R. Mehrabian and G. R. Odette, Acta metall. 37, 2969 (1989).

[7] P. Hing and G. W. Groves, J. Mater. Sci. 7, 427 (1972).

[8] B, D. Flinn, M. Ruhle and A. G. Evans, Acta metall. 37, 3001(1989)

[9] V. I. Kazmin, S. T. Mileiko and V. V. Tvardovsky, Comp. Sci. Tech. 38, (1990)

[10] L. S. Sigl, P. A. Mataga, B. J. Dalgleish and A. G. Evans, Acta metall. 36, 945 (1988).

[11] S.P. Badwal, M.J. Bannister, R.H.J. Hannink (Eds.), Science and Technology of Zirconia V, Technomic Pub. Co., Lancaster, Pennsylvania, 1993.

[12] T.B. Massalski (Ed.), Zirconia polymorphism. Binary Alloys Phase Diagrams, Second Edition, ASM International, Materials Park, Ohio 3 (1990) 2940-1.

[13] M. H. Yanagida, K. Koumoto, M. Miyayama, The Chemistry of Ceramics, 1st ed, John Wiley & Sons, Chicester, 1996. [4] I.A. Yashchishyn, A.M. Korduban, V.V. Trachevskii, T.E. Konstantinova, I.A. Danilenko, G.K. Volkova, I.K. Noselev,XPS and ESR spectroscopy of $ZrO2-Y2O3-Cr2O3$ nanopowders, Functional Materials 17 (2010) 306−10. Diffusion Foundations Vol. 1169

[14] Belova I, Öchsner A, Murch GE. Diffusion in Advanced Materials. Durnten-Zurich: Trans Tech Publications; 2014. Accessed November 5, 2018.

[15] R.H.R. Castro, in: R.H.R. Castro, K. van Benthem (Eds.) Sintering (Engineering Materials vol. 35), Springer Verlag, Berlin, Heidelberg, 2013, pp. 1–16.

[16] DE Ultrasonic Devices to Disperse Nanomaterials. (n.d.). doi: https://www.hielscher.com/nano_01.htm

[17] A. Brenner, G.E. Riddell, J. Res. Nat. Bureau Stand. 37 (1946) 31–34.

[18] A. Brenner, G.E. Riddell, Proc. Am. Electropl. Soc. 33 (1946) 16–19.

[19] A. Brenner, G. Riddell, Proc. Am. Electropl. Soc. 34 (1947) 156–159.

[20] A. Brenner, G.E. Riddell, J. Res. Nat. Bureau Stand. 39 (1947) 385–395.

[21] A. Brenner, Met. Finish. 52 (11) (1954) 68–76.

[22] G. Mallory, Plating 61 (1974) 1005–1014.

[23] B. D. FLINN, M. RmLEf and A. G. EVANS, Acta metalL Vol. 37, No. 11, pp. 3001-3006, 1989

[24] M. Omori, Materials Science and Engineering A 287 (2000) 183.

[25] M. Tokita, Journal of the Society of Powder Technology 30 (1993) 790.

[26] Z.A. Munir, U. Anselmi-Tamburini, M. Ohyanagi, Journal of Materials Science 41 (2006) 763.

[27] U. Anselmi-Tamburini et al., Materials Science and Engineering A 394 (2005) 139.

[28] W. Chen et al., Materials Science and Engineering A 394 (2005) 132.

[29] Parissa Nassary Zadeh et al., Flexural strength, fracture toughness and translucency of cubic/tetragonal zirconia materials, The Journal of Prosthetic Dentistry, 2018, ISSN 0022-3913, https://doi.org/10.1016/j.prosdent.2017.12.021

[30] M. Aboushahba et al., Future Dental Journal 4 (2018) 76-83

[31] Wang, Kun & Li, Chong & Gao, Yonghui & Lu, Xionggang & Ding, Weizhong. (2009). Thermodynamic reassessment of ZrO2-CaO system. Journal of the American Ceramic Society. 92. 1098-1104.

[32] Miquel Turon-Vinas, Marc Anglada, Strength and fracture toughness of zirconia dental ceramics, Dental Materials, Volume 34, Issue 3, 2018, Pages 365-375, ISSN 0109-5641, https://doi.org/10.1016/j.dental.2017.12.007.

[33] Kyocera. "Zirconia (Zirconium Oxide, ZrO2) | Fine Ceramics (Advanced Ceramics) | KYOCERA." KYOCERA GROUP GLOBAL SITE, global.kyocera.com/prdct/fc/list/material/zirconia/zirconia.html.

[34] Wenlong Yao, Jing Liu, Troy B. Holland, Lin Huang, Yuhong Xiong, Julie M. Schoenung and Amiya K. Mukherjee, Scripta Materialia 65 (2011) 143–146

[35] Rocha-Rangel, Enrique. (2011). Fracture Toughness Determinations by Means of Indentation Fracture. 10.5772/18127.